Memristor circuits for colloidal robotics: Temporal access to memory, sensing, and actuation

Jing Fan Yang[1], Albert Tianxiang Liu[1,2], Thomas A. Berrueta[3], Ge Zhang[1], Allan M. Brooks[1], Volodymyr B. Koman[1], Sungyun Yang[1], Xun Gong[1], Todd D. Murphey[3], and Michael S. Strano[1*]

[1]Department of Chemical Engineering, Massachusetts Institute of Technology, Cambridge, MA 02139, USA
[2]Department of Molecular and Cellular Physiology, School of Medicine, Stanford University, Stanford, CA 94305, USA
[3]Department of Mechanical Engineering, Northwestern University, Evanston, IL 60208, USA
[*]Corresponding author. Email: strano@mit.edu

Abstract

Micrometer-scale robots capable of navigating enclosed spaces and remote locations are approaching reality. However, true autonomy remains an open challenge despite substantial progress made with externally supervised and manipulated systems. To accelerate the development of autonomous microrobots, we seek alternatives to conventional top-down lithography. Such additive technologies like printing, coating, and colloidal self-assembly allows for rapid prototyping and access to novel materials, such as polymers, bio- and nanomaterials. On the basis of recent experimental findings that memristive networks can be rapidly printed and lifted off as electronic microparticles, we introduce an alternative design paradigm based on arrays of two-terminal memristive elements that enables real-time use of memory, sensing, and actuation in microrobots. We validate several memristor-based designs representing key building blocks towards robotic autonomy: tracking elapsed time, timestamping a rare event, continuously cataloguing time-indexed data, and accessing the collected information for a feedback-controlled response as in a robotic glucose-responsive insulin, as a test problem. Our computational results establish an actionable framework for microrobotic design – Tasks normally requiring complex circuits can now be achieved with self-assembled and printed memristor arrays within microparticles.

This is the author manuscript accepted for publication and has undergone full peer review but has not been through the copyediting, typesetting, pagination and proofreading process, which may lead to differences between this version and the Version of Record. Please cite this article as doi: 10.1002/aisy.202100205.

Introduction

The potential impact of robots capable of realizing *sense-think-act* cycles at the micrometer scale has been widely appreciated across fields for decades [1–3]. While recent work has made strides in supervising and actuating micromachines externally using light [4,5], sound [6,7], and magnetic/electric fields [8–10], complementary progress towards fully autonomous and tetherless agents has been more gradual [11]. To date, the critical challenge of integrating various on-board microscale components [12] has been targeted using integrated circuit (IC) microfabrication. As an alternative, recent experimental findings have shown that parallel arrays of memristors can be rapidly printed *en masse* and lifted-off as a microparticle swarm with the use of facile additive technologies. Based on these results, we present and validate the design of an alternative memristor-based circuit architecture compatible with additive fabrication methods and emerging materials. Our materials-based design of on-board electronics enables untethered autonomous microrobots to sense, think, and act via temporal access to on-board sensing, memory, and actuation. These capabilities embody surprisingly powerful computation within a simple circuit comprising only two-terminal resistive elements.

Over the course of miniaturizing macroscopic robotics to centi- and millimeter scales, innovations in individual robotic components such as actuators [13–15], controllers [16], and power electronics [17,18] have proven critical, exemplified by the recent autonomous flight of an insect-sized robot [19]. These improved components are still tied together by on-board IC chips in miniature robots, unchanged from their larger-scale counterparts [20,21].

On the other hand, IC chips are less common in microrobots, or colloidal robots, which we define as micrometer-scale robots that can be dispersed in a fluid [22]. To this end, a few research groups have fabricated sophisticated immobile sensor nodes [23–26] that exceed 250 μm in size and are externally supervised or monitored, with key tasks outsourced off-board such as recording of the sensed information. The infrequent breakthroughs in this area are contrasted with a rich body of literature on actuation [4,27–30], locomotion [31–35], energy harvesting/storage [36,37], and sensing modules [38–41] for autonomous colloidal robotics. These components, which often tolerate a lower fabrication resolution but require IC-incompatible novel materials, present an opportunity for emerging fabrication platforms like inkjet printing [38,42–44], screen printing [45,46], stamping [47], and colloidal self-assembly [48,49]. Naturally, an accompanying micrometer-resolution construct is needed to integrate and coordinate the individual robotic functionalities on a micron-sized entity.

To this end, there have been efforts towards robotic components that are inherently dual-functional. For example, sensing is integrated with actuation [29] or locomotion [50] using responsive materials, which have found wide applicability in autonomous targeted delivery [51–53]. Nonetheless, tasks such as autonomous data gathering remain challenging with intrinsic material properties alone. On the other front, self-propelled micromotors can develop additional capabilities as a collective, such as swarming and self-assembly [54]. Advanced collective tasks such as separation and peer recruitment, however, are not yet demonstrated in micrometer-scale systems, as they require coordinated execution of sensing, data processing, memory updating, and actuation steps on-board [55–57].

Moreover, certain robotic components lack a design at the micrometer scale realizable with additive fabrication unlike on-board sensors and actuators. The most prominent example is a timekeeping mechanism, which is essential for feedback control and computation [58–60]. While timekeeping may seem ancillary to autonomy, all Turing-equivalent models of computation rely on sequential logging of states as they evolve [61], which tracking time allows one to do. In the absence of chronometry, basic control-theoretic notions of stability, robustness, and task-performance become impossible to guarantee in any but the most trivial of control problems [62,63]. While there have been relevant efforts based on time-dependent diffusion [64], materials erosion [41], and biological cell activity [65], their temporal information is only communicated to the operator in the end and isolated from other robotic elements, if any. By contrast, temporal access to the memory, sensors, and actuators on-board is desired for microrobots that sense, think, and act autonomously.

Herein, we develop a design framework that allows micron-scale robots to have real-time access to memory, sensing, and actuation. The lean and compact electrical circuit only comprises simple, two-terminal resistive elements: memristors in parallel bridged by fixed or chemiresistors. This dramatic reduction in complexity from conventional microchips thus permits the use of a wide range of micrometer-resolution but facile fabrication technologies. In turn, they expand the arsenal of compatible materials to include polymers, biomaterials, nanoparticles, and their composites [42,66,67]. We computationally study designs that accomplish four autonomous microrobotic tasks of increasing complexity: (i) logging a robot's excursion time; (ii) detecting and timestamping a rare chemical event; (iii) collecting and cataloging a series of time-indexed data; and (iv) accessing the measurement data stored on-board and implementing feedback control, as in a closed-loop insulin delivery system. These results validate our framework based exclusively on two-terminal resistive elements whereby tasks that normally require complex circuit design can be achieved with relatively simple components and connectivity.

Colloidal Robotics Based on Memristors

A memristor is a *memory-resistor* whose resistance is modulated by its current history [68,69], switching between a high- and a low-resistance state (R_{OFF} and R_{ON}, Figure 1A). Each memristor doubles as both a simple two-terminal switch as well as a non-volatile memory bit. Unlike a typical random-access memory, a memristor sustains the stored information without a power source. The switch/memory dual functionality, together with memristors' small footprint and stackability [70], makes possible a compact and energy-efficient electrical circuit compatible with colloidal robotics.

The classical model of a memristor's switching dynamics [68,71–73] is illustrated in Figure 1B: A moving phase boundary partitions a memristor into two interconvertible regions of resistivity R_{OFF} and R_{ON}. A memristor n's instantaneous resistance – or *memristance* – is:

$$M_n(t) = R_{ON} w_n(t) + R_{OFF}\left[1 - w_n(t)\right] \tag{1}$$

where $w_n(t) \in [0, 1]$ is the nondimensionalized location of the partition. When an electrical current $I_n(t)$ passes through the memristor, its dynamics is governed by:

$$\frac{d}{dt} w_n(t) = \frac{\mu R_{ON}}{L^2} I_n(t) \tag{2}$$

for a device of effective length L and an average mobility μ which characterizes the electromigrative drift of the charged dopants. $M_n(t)$ is in turn a function of the entire current history $I_n(0 \rightarrow t)$. The current-voltage relation over a single memristor n (I_n-V_n) takes a nonlinear form:

$$V_n(t) = M_n(t) I_n(t) = \left\{R_{ON} w_n(t) + R_{OFF}\left[1 - w_n(t)\right]\right\} I_n(t)\,, \tag{3}$$

which explains the pinched hysteresis loop in the experimental *I-V* curve in Figure 1A, a key fingerprint of a memristor [74]. If the initial condition is given for w_n and the driving voltage $V_n(t)$ is known, the memristance can be tracked over time by solving the differential equation.

Although a number of more involved memristor models have emerged over the years that include detailed descriptions of the complex microscopic physics [75,76], we base our simulations in this work on the widely-employed classical compact model above, which is proven to be optimal for circuit- and system-level simulations and validation [77,78]. That said, all our results forward hinge only on the most general memristive behaviors, and the conclusions remain true should a different mathematical model be applied.

On-Board Time Awareness

Shown in Figure 1C, the simple memristor array architecture comprises a voltage source V_0., an array of memristors in parallel (M_n, n = 1, 2, 3…), and the interspersing resistors – all two-terminal elements. The simplest task is to record on-board the single variable of *excursion time*, defined as the global time that has passed since the robot's deployment, independent of the events encountered. This passive task can be accomplished without any sensing and actuation functions. In this work, we set V_0 = 1V unless otherwise noted. The voltage may be supplied by either harvested (e.g. a solar cell or a photodiode) or stored energy (e.g. a zinc-air battery), both of which have been miniaturized for sub-100μm-scale applications [5,39,79,80]. While the basic fixed resistors are commonly found in memristor circuits as secondary parasitic electrical elements, for instance to account for the wiring resistance [81], they are essential in our architecture to create the *one-at-a-time switching sequence* that encodes time (Figure 1D): Assuming an initial condition where all memristors are ON ($M_n = R_{ON}$, $\forall n$), any current would preferentially pass through M_1 closest to the energy source. Consequently, M_1 is selectively switched OFF, or at least largely, before the current bypasses the now highly resistive M_1 and starts switching OFF M_2. Likewise, M_3, M_4, and so forth are sequentially shut OFF, thereby encoding the passage of time in the respective memristive states.

We replicate the one-at-a-time switching sequence with circuit simulations of a 7-memristor discrete array (M_n, n = 1 to 7, Methods S1.1). Shown in Figure 1G, the final set of memory states is a function of the excursion time. For example, if we release the autonomous robots are retrieved at t = 144s, the final memristor states read [OFF OFF OFF ON ON ON ON]. In comparison, robots remaining in the environment for a longer 180s report [OFF OFF OFF OFF ON ON ON], since more memristors are switched OFF as time progresses. This mechanism of reading time off the collective memristor states is an exact analogy to the renowned Galileo thermometer (Supplementary Figure S8), for which temperature is encoded as the rise/fall states of a set of floats of varying densities [82].

An array of memristors in parallel can also be fabricated by laying down a continuous layer of memristive ink between two resistive 2D sheets (Figure 1E) via, for instance, inkjet printing [38,83]. Memristive inks have been reported to be made from an array of polymers, composites, and nanoparticles/flakes [39,84]. Our prior experimental works [38,83] show that arrays of electronic particles 20 to 1000μm in size can be stamped out from the sandwich stack *en masse* (Figure 1F, Supplementary Materials S2.4). The technique allows a memristor array to be fabricated altogether via high-throughput coating or printing [85,86], saving the trouble of defining discrete memristors and interconnects. This continuous implementation is represented by a mathematical model built upon the single memristor dynamics and cable theory (Methods S1.2). We numerically simulate the resultant coupled partial differential equations with the method of lines. Figure 1H shows the same sequential switching behavior observed in the discrete simulations. In this case, location of the spatial boundary between ON-state memristors and those switched OFF marks the excursion time. As time passes, an increasing portion of the memristive layer adopts the highly resistive state. The ON/OFF boundary thus propagates further away from V_0 with time. Experimentally, the boundary's location would be marked by an abrupt drop in the local cross-plane resistance, which can be pinpointed by sampling with a basic probe [38].

The readout variability introduced by measuring the memristor states is an important practical consideration. Similarly, cost-effective additive fabrication platforms such as printing and coating may introduce a higher degree of device variability as compared to lithography, where uniformity is an ultimate pursuit. To test our design's robustness to variations, we simulate large populations of discrete memristor arrays with a series of variabilities in their intrinsic ON-state memristance R_{ON}, fixed resistor resistivity R_R, voltage supply V_0, or extrinsic measurement accuracy. Assuming normal distribution, we draw 400 samples for each level of relative standard deviation (0 to 20%) and for each of the four parameters. The data presented in Figure 1I state that even with a large variability of 20% in any of the parameters, accurate excursion time is read from at least 56.0% of the arrays. Since autonomous cell-sized robots are by default deployed in sizable batches, an accurate collective readout is affirmed so long as the majority (> 50%) report the same reading. In other words, this memristor array is robust to more than 20% of intrinsic and extrinsic variabilities. To put this

wide error tolerance in perspective, the relative variation in R_{ON} can be consistently controlled below 8% in the latest spin-coated memristor devices of a wide range of materials [87–90].

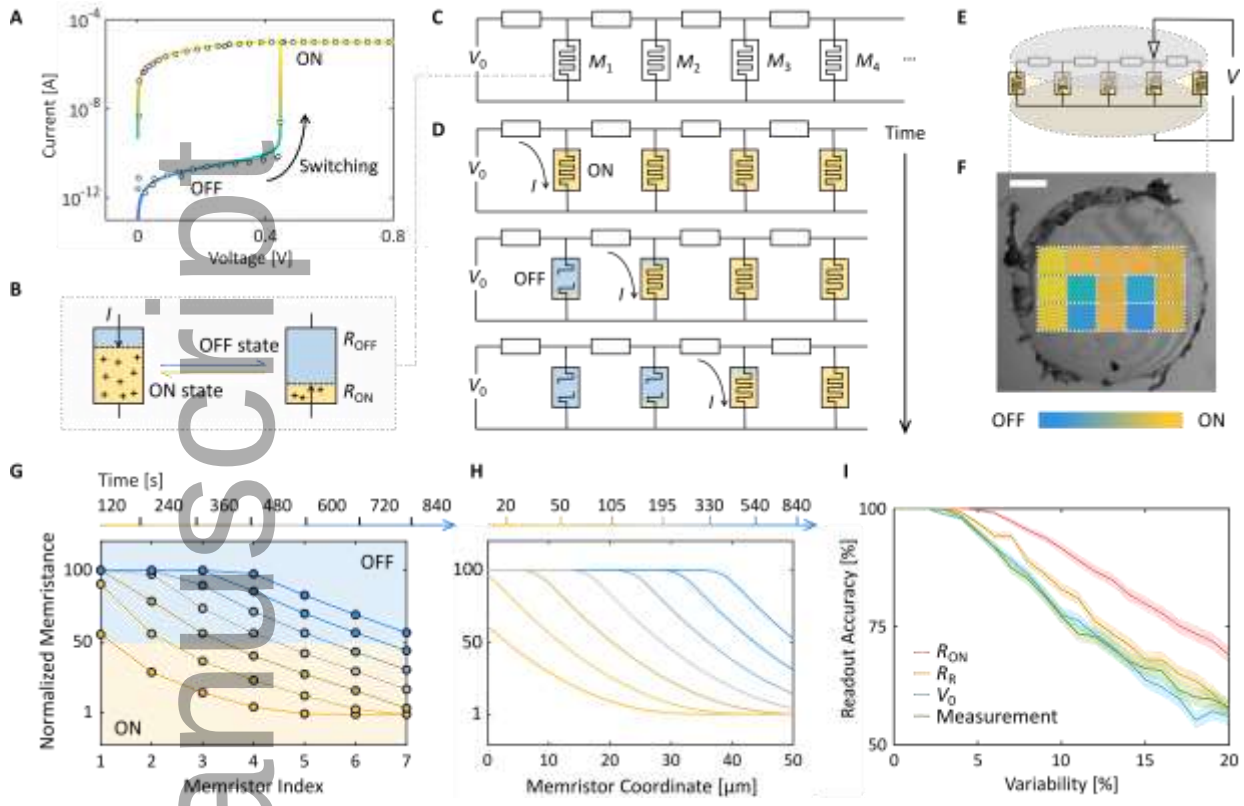

Figure 1. (A) The experimental (circles) and simulated (colored curve) I-V relations of a representative memristor which is switched from OFF to ON. Experimental data digitized from Ref. [91]. The memristance ranges from 37.5kΩ (ON, yellow) to 10GΩ (OFF, blue). (B) The classical model of a single memristor's switching dynamics, in which the memristor is turned OFF or ON as a current I shifts the phase boundary. (C) The memristor array architecture which comprises an energy input V_0, memristors M_n in parallel bridged by either fixed resistors for logging excursion time or chemiresistors as sensors. (D) The sequential switching phenomenon along a memristor array illustrated. As time elapses, the initially ON memristors are switched OFF sequentially. The final memristor states therefore encode time. (E) Literature has shown that a continuous matrix of memristive ink material printed or coated between resistive 2D sheets is equivalent to an array of memristors in parallel. (F) On a particle stamped out from the sandwich stack, different regions of the continuous memristive layer can be selectively switched ON/OFF by an applied voltage with the currents diffusing slowly. Scale bar, 50μm. Data adapted from Ref. [38]. (G) Simulated normalized memristance of 7 discrete memristors in parallel. Memristors are sequentially switched OFF as time elapses. V_0 = 1V, μ/L^2 = 1s^{-1}V^{-1}, α = R_{OFF}/R_{ON} = 100. (H) Simulated normalized memristance of a continuous memristor array. The switched OFF region of the memristive layer expands over time. V_0 = 1V, μ/L^2 = 1s^{-1}V^{-1}, R_R = 1.75kΩ/μm, α = 100. (I) Even with a high variability in R_{ON}, R_R, V_0, or with a high measurement error of 20%, the majority of the 400 simulated memristor arrays report the correct excursion time. As microrobots are deployed and retrieved in batches, this allows the correct time to be interpreted.

Detecting and Timestamping a Rare Event

In addition to passively recording the excursion time, a microrobot with basic sensors should allow its history to be tracked. In the example scenario illustrated in Figure 2A, a robot travels down a pipeline where the oxygen concentration is low throughout except for a leaky region. The leak's location and length are of interest.

We integrate the sensing capability with timing and memory by simply substituting the fixed resistors in Figure 1C with chemiresistors, whose conductance is modulated by the concentration of an analyte. Chemiresistors have already been used in cell-sized robots as a sensing device. Examples include ammonia and triethylamine sensors fabricated from just a sheet of MoS_2 monolayer [39,92]. The rich literature of chemiresistive materials offers solution to sense pH, metal ions, biomolecules, as well as small and large gas molecules with a relative resistivity change (the response ratio) of up to several thousands [93–95].

In a memristor array, if the circuit's chemiresistance increases as a response to a change in the local chemical environment, sequential switching of the parallel memristors slows down and vice versa. With a high chemiresistor sensitivity, the presence of an analyte beyond a threshold can in essence pause subsequent switching, and in turn pause the propagation of the ON/OFF boundary seen in Figure 1H above. The chemiresistors may be *reversible*, meaning they resume the pristine resistance once the analyte is no longer sensed. The discrepancy between the time recorded by this array and the excursion time therefore signals the duration of exposure to a high analyte concentration. On the other hand, the halt to memristor switching is permanent if the analyte binds *irreversibly* to the chemiresistors as in the case of the aforementioned MoS_2 sensing surface [39]. The very instant of entering the analyte-rich region is thus frozen in this case. As a result, the tri-array configuration in Figure 2B records the onset time of a sensing event, its duration, and the excursion time respectively with memristors bridged via irreversible chemiresistors, reversible chemiresistors, and fixed resistors. On the contrary, if a lower-than-usual chemical concentration is to be detected, there are chemiresistors of inverted responsiveness available that are only conductive under sufficient analyte exposure [94].

Figure 2C shows the circuit simulation results for the pipeline leak scenario, where the memristor arrays together detect and timestamp a sensing event. Before the robot enters the leaky region, memristor arrays with reversible and irreversible chemiresistors behave identically to an ordinary, non-responsive array (left panels, t = 100s). Upon entering the leaky region, however, arrays with chemiresistors paused as the excursion time advances (center panels, t = 320s). Of the two, only the array with reversible chemiresistors (green) is released from the interruption after the robot travels past the leak after t = 320s. The simulation in the right panels shows that, of the 450s excursion time, eventually, the irreversible array (red) clocks only the 100s preceding the leaky region, whereas the reversible array clocks 230s: 100s prior to as well as 130s after experiencing the leak. That is, from the final memristor array states, we can extract the robot's temporal history regarding the sensing event – in this case an onset at t = 100s and a duration Δt = 220s. With the average longitudinal velocity computed from the pipeline length and the excursion time, the temporal information can then be translated into the leak location and length. While we focus on probing the chemical micro-environment here, the local temperature, pressure, and presence of light may be detected as well by substituting the chemiresistors with thermistors, force-sensing resistors, or photoresistors, all of which printing-compatible or solution-processable [96–98].

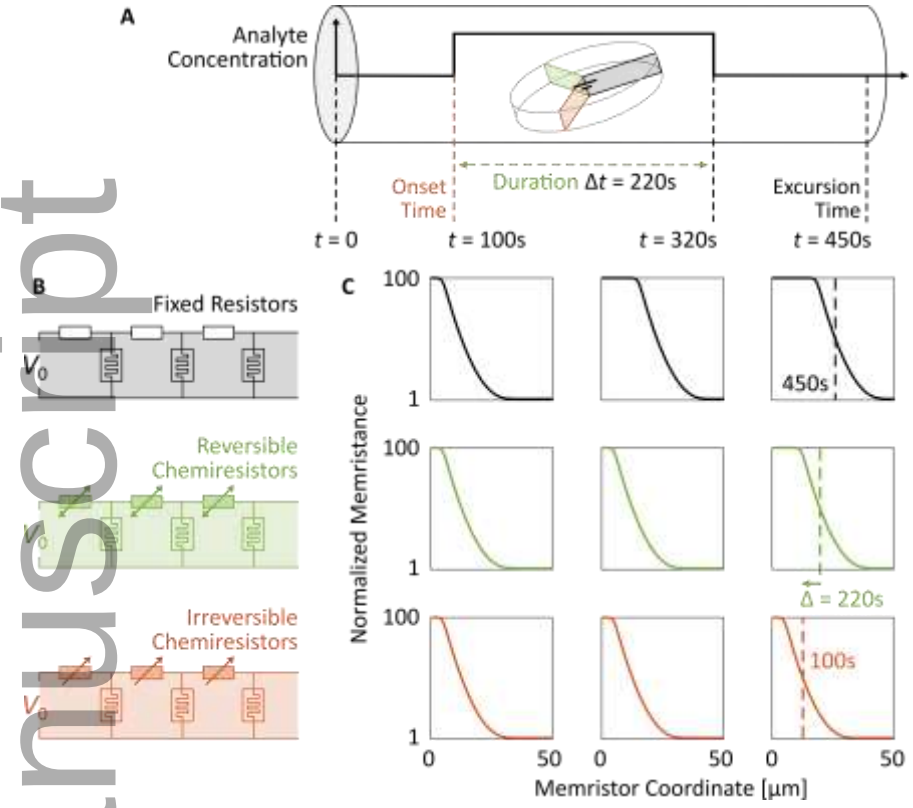

Figure 2. (A) Illustration of a sensing robot traveling down a pipeline with an oxygen-rich leak region to be detected and reported. (B) Memristor arrays with fixed resistors, reversible chemiresistors, and irreversible chemiresistors. (C) Memristor states of the three respective arrays (top down: black, green, and red) at t = 100s, 320s, and 450s (left to right), which corresponds to the time right before the robot enters the leak region, exits the leak region, and ends the voyage. The panel for t = 450s shows that the final memristor states allow the excursion time, the duration, and the onset time to be extracted, and in turn location and length of the leak. V_0 = 1V, μ/L^2 = 1 $s^{-1}V^{-1}$, α = 100, oxygen concentration $[O_2]$ = 250ppm for $t \in$ [100s, 320s] and 0 otherwise. The chemiresistor response $R_R([O_2])$ follows that described in Ref. [99].

Extension to Multivariable Sensing

We expanded upon the 1D time-recording array design above for logging multi-variable information in the form of a 2D set of memristor states. A 2D memristor array further exploits the planarity of electronic microparticles stamped out of a continuous sandwich stack, previously seen in Figure 1F (Supplementary Materials S2.4). A multi-variable sensing robot allows, for instance, detection of the locations and sizes of an unknown number of separate leaks (Supplementary Figure S12), or more generally registration of time-indexed data of the immediate surroundings. As an example, Figure 3A presents a scenario where an enclosed space's spatial distribution of an analyte is to be probed in the form of time-concentration tuples.

The 2D architecture in Figure 3B consists of a series of 1D sensing arrays branching out along the y axis from another 1D memristor array with fixed resistors (the *trunk*) along the x axis. As demonstrated by the schematics and simulation results in Figure 3B-E (Methods S1.3), the trunk memristors are sequentially shut OFF as time progresses, successively delivering electric voltage to the branches further away. Meanwhile, a *circuit breaker* memristor joins each branch to the trunk. A short while after a branch is delivered power, this circuit breaker is switched OFF, thereby blocking further current flow. The non-volatile memristors on the branch are thus frozen thereafter. The overall effect is a sequential activation of the branch arrays along y, each activated for only a short time window.

From the perspective of a single memristor branch, it is powered only after some time t as the trunk memristors switch progressively along x. The memristors on this branch then start to sequentially switch OFF for Δt, the timescale of switching a circuit breaker. Importantly, because the speed of sequential

memristor switching along a branch is modulated by the chemiresistance, the extent each branch is turned OFF during Δt is a monotonic function of the instantaneous analyte concentration in the local environment. The concentrations experienced by the colloidal robot at t_1, t_2, t_3, *etc.* can be quantitatively read out from the respective branches. The two dimensions of the memristor state map (the branches along y and trunk along x) therefore encode the two variables of data we collect (analyte concentration and time, respectively), as seen in Figure 3F and Supplementary Video 1. The full 2D circuit simulation shown corroborates the design concept: The hypothesized sinusoidal profile (the solid curve) is very well matched by the memristor states of the array (the 2D map overlaid underneath). In the case of a realistic time trajectory recorded in a jacketed continuously stirred tank reactor [100,101], the memristor array readout again conforms to the actual concentration profile (Figure 3G), suggesting that colloidal robots equipped with a 2D memristor array could function as ubiquitous, mobile sensor nodes within otherwise inaccessible chemical and bioreactors.

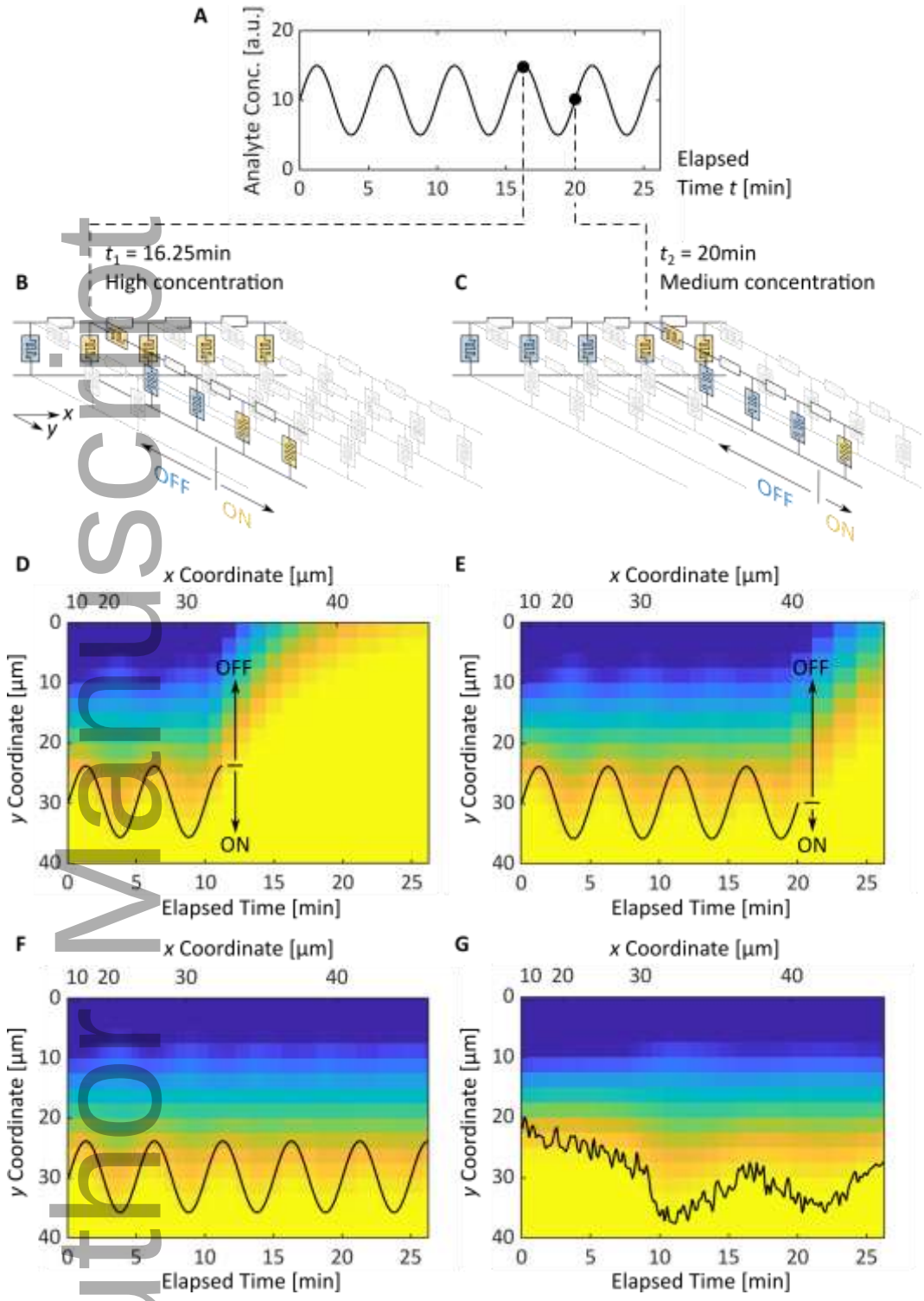

Figure 3. (A) An example of a colloidal robot's history to be recovered from the 2D memristor states. (B, C) Schematics of the 2D memristor array architecture at t = 16.25min and 20min, when the robot detected a high and medium concentration of analyte, respectively. The different concentrations are reflected in the corresponding branches as the different extent of switching. Blue, OFF; yellow, ON. α = 200. (D, E) The 2D memristor states at t = 16.25min and 20min. The branches are sequentially activated over time, and each encoding the analyte concentration of a certain t. (F, G) The final 2D memristor states of a robot experiencing a sinusoidal and realistic analyte profile, respectively. The profiles overlaid on top as solid curves conform well to memristor array readouts. Parameter values used in the simulations are listed in Methods S1.3.

Feedback-Controlled Autonomous Drug Delivery

As an example of more complex colloidal robotic tasks of biomedical relevance, we consider intelligent cargo delivery. Many works have shown that it can be accomplished at high precision via external

supervision and control [9,27,32,102], well suited for short-term biomedical applications [11]. Complementarily, for scenarios where external communication or localization is difficult, or where the robots carry out long-term missions, autonomy is valuable.

Some passive drug delivery systems are occasionally referred to as autonomous microrobots. They are typically polymeric particles responsive to local cues such as abnormal pH or certain biomolecules [103,104]. For example, a *glucose-responsive insulin* (GRI) analogue circulates through a diabetic patient's body unsupervised, releasing doses of insulin whenever the local blood glucose (BG) level – a chemical cue – spikes. The GRI's autonomy liberates the patients from the burden of constant monitoring and painful injections [105–107]. Compared to the autonomy, however, the adaptability and modularity of these particles are limited. Using the GRI as a model engineering application, we instead dock the memristor array circuit with an *electric* actuation mechanism found in immobile *implantable chips*. Such an actuation scheme allows for scheduled dosing of multiple medications [108–110], and the clean-cut electric switching enables controlled and pulsatile delivery [108,111]. Our architecture is illustrated in Figure 4A, where a drug-loaded electric actuation module accesses a memristor array's time-indexed data and delivers cargo accordingly.

In an inhomogeneous environment, the analyte's instantaneous local concentration modulates the memristive states on the corresponding branch. Beyond (below) a threshold concentration (e.g., of glucose, $[G]_{th}$), memristors on the entire said branch would be switched OFF if equipped with chemiresistors that are conductive at a higher (lower) concentration. If so, the voltage at the terminus reaches a threshold V_{th} and actuates the release of a cargo electrically from either an electroactive polymer pocket [112] or a microreservoir [113,114]. Loading drugs into reversible electroactive polymers is a standard procedure in the literature [115]. Therefore, a glucose-sensing memristor array coupled with an insulin-loaded reservoir compose a microrobotic GRI, which we simulate as a proof-of-concept.

We confirm the feasibility of the microrobotic GRI concept via *in silico* pharmacokinetic modeling with PAMERAH [116], a published full-body diabetes model trained with rodent data (Methods S1.4, Supplementary Figure S3). Given any user-specified reservoir kinetics, PAMERAH translates the electrical response of a memristor circuit into a diabetic subject's BG trajectory. Figure 4B(i) shows one such trajectory corresponding to a particular memristor array with an insulin load of 0.018IU, a reservoir release half-life $t_{1/2}$ of 6h, and $[G]_{th}$ = 225mg/dL. The simulated colloidal robot performs adequately as a GRI: Initially with a BG beyond the 240-mg/dL hyperglycemic limit [117], the electrified reservoir releases insulin into the surrounding bloodstream. Owing to the quick release kinetics, the GRI is able to bring the BG down to the non-threatening range within 2 hours – an important criterion for good GRIs [118]. By reversibly pausing the release whenever BG drops below $[G]_{th}$, the microrobotic GRI also prevents overdoses of insulin at all times (signified by BG < 75mg/dL), which may lead to dangerous and sometimes fatal hypoglycemia [119,120]. The memristor array maintained the BG at a healthy level throughout the 24-hour period, during which it effectively suppressed three postprandial (*after meal*) glucose excursions within 2 hours.

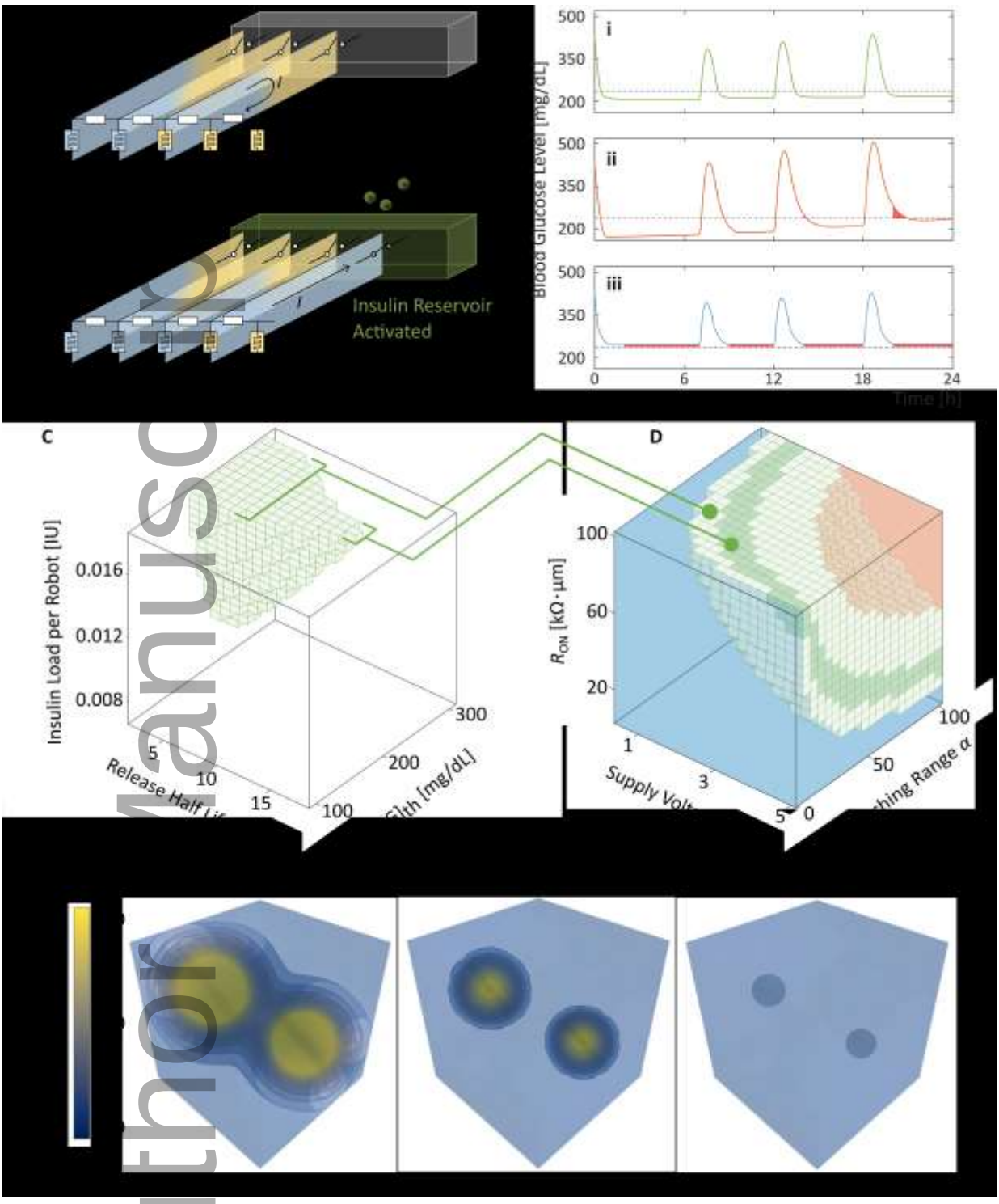

Figure 4. (A) A microrobotic glucose-responsive insulin module can be built by appending a reversible voltage-actuated insulin reservoir to the end of the memristor branches. When the chemiresistors detect a glucose concentration higher than the threshold $[G]_{th}$, the reservoir is activated and vice versa. (B) Representative trajectories of a diabetic subject's blood glucose level in response to a microrobotic GRI of (i) adequate, (ii) low, and (iii) high $[G]_{th}$ of 225, 175, and 300mg/dL respectively. The deviations from an adequate GRI are highlighted in red. The three spikes in each trajectory correspond to BG hikes after meals. (C) Pharmacokinetic modeling facilitates design of the microrobotic GRIs by finding constraints for a qualified GRI on $[G]_{th}$, insulin load, and the release half-life $t_{1/2}$. (D) The GRI constraints are translated to optimal ranges of the memristor array's circuit parameters (V_0, R_{ON}, and α) via circuit simulations. (E) Spatiotemporal simulation of a swarm of 100 microrobotic GRIs responding to spatially localized BG spikes with $[G]_{th}$ of 225 mg/dL. The combination of closed-loop insulin release and ergodic diffusion allows the microrobot swarm to regulate complex spatial distributions of glucose without the need for large amounts of computation.

Moreover, we can optimize the memristor array for a maximized GRI efficacy via scanning the parameter space with parallel runs of PAMERAH (Figure 4C). The scan returns the constraints on $[G]_{th}$ for an adequate GRI performance: Given a load of 0.018IU and a $t_{1/2}$ of 6h, the memristor array should be designed such that

$[G]_{th}$ falls between 180 and 290mg/dL. For a longer $t_{1/2}$ of 12h, the sluggishness in insulin release must be compensated by a tighter requirement on $[G]_{th}$ (210 to 240mg/dL) as shown. Figure 4B(ii) and (iii) exemplify poor GRIs corresponding to glucose thresholds below and over the optimal range, leading to premature depletion of insulin and weak BG regulation, respectively.

The GRI parameter requirements extracted from PAMERAH are translated by circuit simulations into targets for array parameters like V_0, R_{ON}, and the switching range $\alpha = R_{OFF}/R_{ON}$. They are the upstream knobs one turns when designing the robot. Regions shaded dark green in Figure 4D encompass the permissible combinations of V_0, R_{ON}, and α that yield a desired $[G]_{th}$ for a $t_{1/2}$ of 12h. Relaxed constraints on $[G]_{th}$ imposed by $t_{1/2}$ of 6h in comparison translate to wider ranges of circuit parameters, shown in light green. The geometry, which resembles a fragment of a melon rind, is expected: Combinations of high V_0, R_{ON}, and α (shaded red) result in fast switching along a memristor array branch. The insulin release is triggered prematurely at a lower-than-desired BG, corresponding to the oversensitive and non-lasting GRI in Figure 4B(ii). The opposite extreme, shaded blue, conversely yields a threshold too high and a GRI not adequately responsive (Figure 4B(iii)). The simulation workflow, as demonstrated here and sketched as Supplementary Figure S3, forms a complete sandbox for testing and optimizing memristor array designs before any physical prototype is built.

PAMERAH addresses the GRI's system-level performance by modeling the full-body physiology as a network of spatially uniform compartments. On the other hand, the spatiotemporal simulations of a swarm of 100 GRI microrobots show that their ergodic diffusion alone creates the coverage required to regulate complex distributions of glucose without the need for large amounts of on-board computation (Figure 4E, Supplementary Figure S13, and Methods S1.5). In the absence of glucose or insulin diffusion, the inhomogenously hyperglycemic environment at $t = 0$ evolves over time until the BG level universally drops to the healthy range.

The GRI simulations are a proof-of-concept demonstration of how a memristor array enables autonomous cargo delivery via a feedback-controlled response to its surroundings. Thinking further, we anticipate the memristor array platform to enable even more diverse cargo delivery programs and beyond. For example, irreversibly activated reservoirs, such as an electrodeposited polypyrrole film [112], could enable the administration of an emergency pulse of epinephrine when a large amount of allergen is picked up by the chemiresistor sensors. Substituting a GRI's positive chemiresistors with negative ones, and hence establishing a lower threshold for glucose, offers a viable path towards glucose-responsive glucagon delivery for hypoglycemia prevention [120]. The memristor array also offers a means to responsively administer multiple drugs either simultaneously or sequentially, all the while recording the analyte concentration as memristor states. The sequential, scheduled delivery is a particularly relevant application in the field of chronotherapeutics [121,122], which adapts the treatment according to the patient's circadian rhythms via, for instance, separate day and night regimens.

Discussion

In this computational study, we design and demonstrate the capabilities of memristor-based arrays that integrate timing, memory, sensing, and actuation on-board micrometer-scale robots. Instead of miniaturizing the existing electronics used in macroscale robotics, we show that the distinct functionalities can be combined into one lean circuit comprising only two-terminal resistive elements; Among them, the memristors register to the memory, chemiresistors sense analytes, and they collaboratively translate time into measurable resistance states. Throughout the study, we make sure the design is accessible to a diverse assortment of technology platforms and material systems, opening up avenues for high-throughput fabrication of complex autonomous robots from inexpensive printing, stamping, and coating techniques. The simplest array may be constructed by just laying down a continuous layer of memristive film between sheet electrodes. Our simulations further show that the potential variabilities in array fabrication and measurement are not a major concern thanks to an error tolerance exceeding 20%.

It is worth noting that while the memristive switching process is increasingly well understood in terms of the microscopic physics and chemistry, the time-dependent switching dynamics is rarely considered for engineering applications. Its pivotal role in our array's on-board awareness of time elevates memristors beyond the role of individual datum-storage units in microrobotics. Interestingly, as time is encoded spatially and sequentially thanks to the delay introduced by each memristor, our design is well compatible with slow-acting, non-state-of-the-art memristors which are otherwise considered unsuitable for computing tasks [123].

Beyond the basic task of registering the excursion time, we devise three extensions to the minimal array to enable advanced capabilities not yet available to autonomous microrobotics. Based upon prior reports of using reversible and irreversible chemiresistors as on-board sensor elements, we design an array that senses and timestamps a major event, for instance encountering an oxygen-rich leak of unknown location and size in a remote pipeline. Leveraging the planar nature of patterning platforms, we expand the minimal array to two dimensions for collection and cataloging time-indexed data, such as the time trajectory of a pollutant's concentration. Finally, since the sensing, memory, and timing functions all communicate via electrical signals, the sensor data stored on-board is readily accessible to additional robotic components. As we quantitatively confirm with circuit simulation and pharmacokinetic modeling, this allows an electroactive polymer module to deliver insulin in a glucose-responsive and/or scheduled manner within a diabetic patient.

Looking further, as we consider tasks that extend beyond those illustrated, circuits of more involved topologies and connectivity within the planar memristor matrix can be designed. For tasks that can be expressed as optimization problems, techniques from the fields of combinatorial optimization [124], simulated annealing [125], optimal control [126], and pareto optimization [127] can be used. For complex tasks that cannot be obviously framed as an optimization, recent advances in the reinforcement learning literature can be applied [128]. As memristors are simple two-terminal elements, most automated design approaches will benefit from a substantial complexity reduction relative to circuits based on three-terminal transistors.

We note that this study is illustrative rather than exhaustive. While we examine memristors with the most general switching behavior, certain memristive devices may exhibit experimental non-idealities deviating from the simplest electromigrative drift depiction. For example, conductive-bridging memristors typically require a one-time forming step before the memristors can be repeatably switched ON and OFF [129]. In the context of memristor array operation, skipping this pre-treatment may give rise to faster sequential switching and thus a shorter timing window. Another example is the recently reported "discrete state" memristor whose resistance switches stepwise [130,131]; Our simulations, in contrast, describe a continuously changing "analog" resistance. Interestingly, these discrete state memristors may work even better in a memristor array with a more pronounced and abrupt ON/OFF boundary. If desired, one may mathematically model the details of these non-idealities by, for instance, introducing additional equivalent circuit elements like capacitors and rectifiers [69,132]. As mentioned earlier, however, this report adopts the classical minimal model throughout for its simplicity and suitability for system-level simulation. The model's generality further echoes that our design relies only on the most fundamental feature of memristors – the resistive switching, unaffected by nuances in the mechanisms or material systems. In this study, we also consider each memristor array to experience a uniform chemical concentration across its volume. The approximation is made on the basis that the devices are significantly smaller than the scales of interest in typical microrobotic applications, such as sensing in pipelines and reactors. This treatment is consistent with prior studies on micrometer-sized sensor nodes, both mobile [39,41] and immobile [5,23]. In the presence of a large chemical concentration gradient, however, the approximation may become less valid. One example is the gradient created by an H_2O_2 efflux immediately adjacent to a biological cell [133]. In such cases, micrometer-sized sensors can provide only a fudged average and a qualitative temporal trajectory.

As we seek a general design that applies to diverse materials, we are unable to assert a single quantitative performance metric attainable, such as an ultimate temporal resolution. That said, the connection between material properties (e.g., μ, R_{ON}, and α) can be analyzed with the nondimensionalized model in Supplementary Materials S2.1. Once a particular material system is selected, the temporal resolution of a memristor array is capped by different factors in discrete and continuous arrays. In a discrete array where the

individual memristors are separate, the limiting factor is the number of memristors one can package into a sub-100-μm robot. This is in turn limited by the affordable spatial resolution of the patterning platform, which is on the order of a micrometer for printing, stamping, and colloidal assembly. The limiting role is played by the *measurement* platform's spatial resolution, on the other hand, in the case of a continuous array where the memristors are altogether embedded in a continuous memristive layer. For example, the *x*-*y* stage of a probe station – the traditional platform for memristor measurement – typically offers a resolution of a micrometer. If we use this probe to read the example memristor array in Figure 1H, the temporal resolution can be as small as ±1.8s for a time window of 15s and shorter. It gradually deteriorates, however, to ±26.3s after the cell-sized robot is stationed in the environment for 400s (Supplementary Figure S6), a consequence of the decelerating sequential switching which is visible in Figure 1H and further analyzed in Supplementary Materials S2.1. The deceleration thus limits the array's worst-case temporal resolution and is mathematically a direct result of the uniform fixed resistors and constant voltage. As an alternative to the probe station, conductive atomic force microscope has become a common tool for memristor characterization [131,134,135], offering reduced measurement errors and more importantly, a nanometer-range resolution [136,137]. This, then, translates to a temporal resolution of merely ±0.03s at t = 400s in the same benchmarking array simulated. As further analyzed in Supplementary Materials S2.3 and Supplementary Table S3, memristor array circuits may be designed and proper measurement platforms selected to suit the temporal resolution demands of specific applications, such as sensing within a microfluidic channel, an industrial-scale flow reactor, and the digestive system.

Lastly, while circuit simulations have been proven to be trustworthy and indispensable to modern circuit design [138], experimental verifications are important in the case of microrobotics – a field at the intersection of engineering, physics, chemistry, and sometimes biology. For instance, experiments are needed to evaluate the stability of the memristors and chemiresistors over prolonged exposure to the environment, which has been studied in air but not yet in solution. The uncertain effects of unwanted absorbates, particle edges, and analyte diffusion on the sequential switching phenomenon should also be elucidated. Looking further, we see this work paving the way towards tools for multi-robot control, robot-to-robot communication, as well as self-organization and swarming – some of the key open questions identified in microrobotics [139].

Acknowledgement

We thank D. Randall, A. W. Richa, D. I. Goldman, T. Palacios, J. England, A. Pervan, J. Daymude, and M. Hempel for helpful discussions.

Funding

This work was supported by the Army Research Office through the MURI grant for Formal Foundations of Algorithmic Matter and Emergent Computation (W911NF-19-1-0233). Ge Zhang acknowledges support from MathWorks Inc. through the MathWorks Engineering Fellowship.

Author contributions

A.T.L., V.B.K., J.F.Y., and M.S.S. outlined the circuit design; J.F.Y., A.T.L., and G.Z. performed circuit simulations; J.F.Y. performed the pharmacokinetic modeling; J.F.Y. performed the robustness analysis; T.A.B. performed the spatiotemporal simulations of GRI swarms; J.F.Y., A.T.L., and M.S.S. wrote the manuscript. M.S.S. guided the overall research program. All authors read and discussed the manuscript.

References

[1] A. Hey, in *Feynman Comput.*, CRC Press, **2018**, pp. 63–76.

[2] P. Fischer, B. J. Nelson, *Sci. Robot.* **2021**, *6*, eabh3168.

[3] M. Sitti, *Nature* **2009**, *458*, 1121.

[4] M. Z. Miskin, A. J. Cortese, K. Dorsey, E. P. Esposito, M. F. Reynolds, Q. Liu, M. Cao, D. A. Muller, P. L. McEuen, I. Cohen, *Nature* **2020**, *584*, 557.

[5] A. J. Cortese, C. L. Smart, T. Wang, M. F. Reynolds, S. L. Norris, Y. Ji, S. Lee, A. Mok, C. Wu, F. Xia, N. I. Ellis, A. C. Molnar, C. Xu, P. L. McEuen, *Proc. Natl. Acad. Sci.* **2020**, *117*, 9173.

[6] B. Esteban-Fernández De Ávila, C. Angell, F. Soto, M. A. Lopez-Ramirez, D. F. Báez, S. Xie, J. Wang, Y. Chen, *ACS Nano* **2016**, *10*, 4997.

[7] V. Garcia-Gradilla, J. Orozco, S. Sattayasamitsathit, F. Soto, F. Kuralay, A. Pourazary, A. Katzenberg, W. Gao, Y. Shen, J. Wang, *ACS Nano* **2013**, *7*, 9232.

[8] W. Hu, G. Z. Lum, M. Mastrangeli, M. Sitti, *Nature* **2018**, *554*, 81.

[9] J. Yu, B. Wang, X. Du, Q. Wang, L. Zhang, *Nat. Commun.* **2018**, *9*, 1.

[10] V. K. Bandari, Y. Nan, D. Karnaushenko, Y. Hong, B. Sun, F. Striggow, D. D. Karnaushenko, C. Becker, M. Faghih, M. Medina-Sánchez, F. Zhu, O. G. Schmidt, *Nat. Electron.* **2020**, *3*, 172.

[11] A. M. Brooks, M. S. Strano, *Nature* **2020**, *584*, 530.

[12] D. Jin, L. Zhang, *Nat. Mach. Intell.* **2020**, *2*, 663.

[13] Y. Tang, C. Chen, A. Khaligh, I. Penskiy, S. Bergbreiter, *IEEE Trans. Power Electron.* **2014**, *29*, 2991.

[14] Y. Chen, H. Zhao, J. Mao, P. Chirarattananon, E. F. Helbling, N. seung P. Hyun, D. R. Clarke, R. J. Wood, *Nature* **2019**, *575*, 324.

[15] H. Suzuki, R. J. Wood, *Nat. Mach. Intell.* **2020**, *2*, 437.

[16] K. Saito, M. Takato, Y. Sekine, F. Uchikoba, *Int. J. Adv. Robot. Syst.* **2012**, *9*, DOI 10.5772/54129.

[17] B. Goldberg, R. Zufferey, N. Doshi, E. F. Helbling, G. Whittredge, M. Kovac, R. J. Wood, *IEEE Robot. Autom. Lett.* **2018**, *3*, 987.

[18] M. Lok, E. F. Helbling, X. Zhang, R. Wood, D. Brooks, G.-Y. Wei, *IEEE Trans. Power Electron.* **2018**, *33*, 3180.

[19] N. T. Jafferis, E. F. Helbling, M. Karpelson, R. J. Wood, *Nature* **2019**, *570*, 491.

[20] W. Savoie, T. A. Berrueta, Z. Jackson, A. Pervan, R. Warkentin, S. Li, T. D. Murphey, K. Wiesenfeld, D. I. Goldman, *Sci. Robot.* **2019**, *4*, eaax4316.

[21] B. Chen, H. Yang, B. Song, D. Meng, X. Yan, Y. Li, Y. Wang, P. Hu, T. Ou, M. Barnell, Q. Wu, H. Wang, W. Wu, *Sci. Robot.* **2020**, *5*, eabb6938.

[22] P. Dario, R. Valleggi, M. C. Carrozza, M. C. Montesi, M. Cocco, *J. Micromechanics Microengineering* **1992**, *2*, 141.

[23] S. Lee, A. J. Cortese, A. Mok, C. Wu, T. Wang, J. U. Park, C. Smart, S. Ghajari, D. Khilwani, S. Sadeghi, Y. Ji, J. H. Goldberg, C. Xu, P. L. McEuen, A. C. Molnar, *J. Microelectromechanical Syst.* **2020**, 1.

[24] S. Lee, A. J. Cortese, A. P. Gandhi, E. R. Agger, P. L. McEuen, A. C. Molnar, *IEEE Trans. Biomed.*

Circuits Syst. **2018**, *12*, 1256.

[25] C. Shi, T. Costa, J. Elloian, Y. Zhang, K. L. Shepard, *IEEE Trans. Biomed. Circuits Syst.* **2020**, *14*, 412.

[26] C. Shi, V. Andino-Pavlovsky, S. A. Lee, T. Costa, J. Elloian, E. E. Konofagou, K. L. Shepard, *Sci. Adv.* **2021**, *7*, 1.

[27] K. Malachowski, M. Jamal, Q. Jin, B. Polat, C. J. Morris, D. H. Gracias, *Nano Lett.* **2014**, *14*, 4164.

[28] W. Xu, Z. Qin, C. T. Chen, H. R. Kwag, Q. Ma, A. Sarkar, M. J. Buehler, D. H. Gracias, *Sci. Adv.* **2017**, *3*, DOI 10.1126/sciadv.1701084.

[29] J. Li, P. Angsantikul, W. Liu, B. Esteban-Fernández de Ávila, S. Thamphiwatana, M. Xu, E. Sandraz, X. Wang, J. Delezuk, W. Gao, L. Zhang, J. Wang, *Angew. Chemie Int. Ed.* **2017**, *56*, 2156.

[30] Q. Liu, W. Wang, M. F. Reynolds, M. C. Cao, M. Z. Miskin, T. A. Arias, D. A. Muller, P. L. McEuen, I. Cohen, *Sci. Robot.* **2021**, *6*, eabe6663.

[31] A. Somasundar, *S*. Ghosh, F. Mohajerani, L. N. Massenburg, T. Yang, P. S. Cremer, D. Velegol, A. Sen, *Nat. Nanotechnol.* **2019**, *14*, 1129.

[32] Y. Alapan, O. Yasa, O. Schauer, J. Giltinan, A. F. Tabak, V. Sourjik, M. Sitti, *Sci. Robot.* **2018**, *3*, eaar4423.

[33] J. Palacci, S. Sacanna, A. Abramian, J. Barral, K. Hanson, A. Y. Grosberg, D. J. Pine, P. M. Chaikin, *Sci. Adv.* **2015**, *1*, e1400214.

[34] L. Dekanovsky, B. Khezri, Z. Rottnerova, F. Novotny, J. Plutnar, M. Pumera, *Nat. Mach. Intell.* **2020**, *2*, 711.

[35] B. Khezri, K. Villa, F. Novotný, Z. Sofer, M. Pumera, *Small* **2020**, *16*, 2002111.

[36] J. Ding, V. R. Challa, M. G. Prasad, F. T. Fisher, in *Sel. Top. Micro/Nano-Robotics Biomed. Appl.*, Springer New York, New York, NY, **2013**, pp. 59–83.

[37] H. Zhang, Z. Qu, H. Tang, X. Wang, R. Koehler, M. Yu, C. Gerhard, Y. Yin, M. Zhu, K. Zhang, O. G. Schmidt, *ACS Energy Lett.* **2021**, 2491.

[38] P. Liu, A. T. Liu, D. Kozawa, J. Dong, J. F. Yang, V. B. Koman, M. Saccone, S. Wang, Y. Son, M. H. Wong, M. S. Strano, *Nat. Mater.* **2018**, *17*, 1005.

[39] V. B. Koman, P. Liu, D. Kozawa, A. T. Liu, A. L. Cottrill, Y. Son, J. A. Lebron, M. S. Strano, *Nat. Nanotechnol.* **2018**, *13*, 819.

[40] C. Vervacke, C. C. Bof Bufon, D. J. Thurmer, O. G. Schmidt, *RSC Adv.* **2014**, *4*, 9723.

[41] M. Hempel, V. Schroeder, C. Park, V. B. Koman, M. Xue, E. McVay, S. Spector, M. Dubey, M. S. Strano, J. Park, J. Kong, T. Palacios, *ACS Nano* **2021**, *15*, 8803.

[42] F. Molina-Lopez, T. Z. Gao, U. Kraft, C. Zhu, T. Öhlund, R. Pfattner, V. R. Feig, Y. Kim, S. Wang, Y. Yun, Z. Bao, *Nat. Commun.* **2019**, *10*, 1.

[43] N. Samardzic, M. Mionic, B. Dakic, H. Hofmann, S. Dautovic, G. Stojanovic, *IEEE Trans. Electron Devices* **2015**, *62*, 1898.

[44] K. J. Yoon, J. W. Han, D. Il Moon, M. L. Seol, M. Meyyappan, H. J. Kim, C. S. Hwang, *Nanoscale Adv.* **2019**, *1*, 2990.

[45] B. J. Carey, J. Z. Ou, R. M. Clark, K. J. Berean, A. Zavabeti, A. S. R. Chesman, S. P. Russo, D. W. M. Lau, Z. Q. Xu, Q. Bao, O. Kevehei, B. C. Gibson, M. D. Dickey, R. B. Kaner, T. Daeneke, K. Kalantar-Zadeh, *Nat. Commun.* **2017**, *8*, 1.

[46] Y. D. Kim, J. Hone, *Nature* **2017**, *544*, 167.

[47] E. P. Yalcintas, K. B. Ozutemiz, T. Cetinkaya, L. Dalloro, C. Majidi, O. B. Ozdoganlar, *Adv. Funct. Mater.* **2019**, *29*, 1.

[48] A. F. Demirörs, P. P. Pillai, B. Kowalczyk, B. A. Grzybowski, *Nature* **2013**, *503*, 99.

[49] A. T. L. Tan, J. Beroz, M. Kolle, A. J. Hart, *Adv. Mater.* **2018**, *30*, 1803620.

[50] V. Magdanz, G. Stoychev, L. Ionov, S. Sanchez, O. G. Schmidt, *Angew. Chemie - Int. Ed.* **2014**, *53*, 2673.

[51] J. Li, B. E.-F. de Ávila, W. Gao, L. Zhang, J. Wang, *Sci. Robot.* **2017**, *2*, DOI 10.1126/scirobotics.aam6431.

[52] J. Li, D. J. Mooney, *Nat. Rev. Mater.* **2016**, *1*, DOI 10.1038/natrevmats.2016.71.

[53] B. Mostaghaci, O. Yasa, J. Zhuang, M. Sitti, *Adv. Sci.* **2017**, *4*, 1.

[54] A. A. Solovev, S. Sanchez, O. G. Schmidt, *Nanoscale* **2013**, *5*, 1284.

[55] S. Cannon, J. J. Daymude, D. Randall, A. W. Richa, in *Proc. 2016 ACM Symp. Princ. Distrib. Comput.*, ACM Press, New York, New York, USA, **2016**, pp. 279–288.

[56] S. Cannon, J. J. Daymude, C. Gokmen, D. Randall, A. W. Richa, *arXiv* **2018**, DOI 10.1145/3212734.3212792.

[57] S. Li, R. Batra, D. Brown, H.-D. Chang, N. Ranganathan, C. Hoberman, D. Rus, H. Lipson, *Nature* **2019**, *567*, 361.

[58] A. Lamperski, N. Cowan, *IEEE Trans. Automat. Contr.* **2015**, 1.

[59] C. Lorand, P. H. Bauer, in *Proc. 2003 Am. Control Conf.*, IEEE, **n.d.**, pp. 3323–3328.

[60] A. Q. Nilles, A. Pervan, T. A. Berrueta, T. D. Murphey, S. M. LaValle, in *Proc. 14th Work. Algorithmic Found. Robot.*, **2021**, pp. 210–226.

[61] A. M. Turing, *Proc. London Math. Soc.* **1937**, *s2-42*, 230.

[62] S. M. LaValle, M. Egerstedt, in *Emergent Probl. Nonlinear Syst. Control*, **2009**, pp. 93–106.

[63] S. M. LaValle, M. B. Egerstedt, in *2007 46th IEEE Conf. Decis. Control*, IEEE, **2007**, pp. 1916–1922.

[64] L. C. Gerber, L. Rosenfeld, Y. Chen, S. K. Y. Tang, *Lab Chip* **2014**, *14*, 4324.

[65] J. Park, J. M. Lim, I. Jung, S.-J. Heo, J. Park, Y. Chang, H. K. Kim, D. Jung, J. H. Yu, S. Min, S. Yoon, S.-R. Cho, T. Park, H. H. Kim, *Cell* **2021**, *184*, 1047.

[66] J. A. Rogers, Z. Bao, M. Meier, A. Dodabalapur, O. J. A. Schueller, G. M. Whitesides, *Synth. Met.* **2000**,

115, 5.

[67] A. G. Kelly, T. Hallam, C. Backes, A. Harvey, A. S. Esmaeily, I. Godwin, J. Coelho, V. Nicolosi, J. Lauth, A. Kulkarni, S. Kinge, L. D. A. Siebbeles, G. S. Duesberg, J. N. Coleman, *Science (80-.).* **2017**, *356*, 69.

[68] D. B. Strukov, G. S. Snider, D. R. Stewart, R. S. Williams, *Nature* **2008**, *453*, 80.

[69] J. J. Yang, M. D. Pickett, X. Li, D. A. A. Ohlberg, D. R. Stewart, R. S. Williams, *Nat. Nanotechnol.* **2008**, *3*, 429.

[70] Z. Wang, H. Wu, G. W. Burr, C. S. Hwang, K. L. Wang, Q. Xia, J. J. Yang, *Nat. Rev. Mater.* **2020**, *5*, 173.

[71] Y. N. Joglekar, S. J. Wolf, *Eur. J. Phys.* **2009**, *30*, 661.

[72] Z. Biolek, D. Biolek, V. Biolková, *Radioengineering* **2009**, *18*, 210.

[73] A. G. Radwan, M. A. Zidan, K. N. Salama, in *Proc. Int. Conf. Microelectron. ICM*, **2010**, pp. 284–287.

[74] L. Chua, *Nanotechnology* **2013**, *24*, DOI 10.1088/0957-4484/24/38/383001.

[75] S. Kim, S. Choi, W. Lu, *ACS Nano* **2014**, *8*, 2369.

[76] A. Padovani, L. Larcher, O. Pirrotta, L. Vandelli, G. Bersuker, *IEEE Trans. Electron Devices* **2015**, *62*, 1998.

[77] W. Sun, B. Gao, M. Chi, Q. Xia, J. J. Yang, H. Qian, H. Wu, *Nat. Commun.* **2019**, *10*, 3453.

[78] R. S. Williams, *Faraday Discuss.* **2019**, *213*, 579.

[79] L. Cao, G. Fang, H. Cao, X. Duan, *Langmuir* **2019**, *35*, 16079.

[80] A. T. Liu, Y. Kunai, A. L. Cottrill, A. Kaplan, G. Zhang, H. Kim, R. S. Mollah, Y. L. Eatmon, M. S. Strano, *Nat. Commun.* **2021**, *12*, 1.

[81] H. Li, P. Huang, B. Gao, B. Chen, X. Liu, J. Kang, *IEEE Electron Device Lett.* **2014**, *35*, 211.

[82] A. Puglisi, A. Sarracino, A. Vulpiani, *Phys. Rep.* **2017**, *709–710*, 1.

[83] A. T. Liu, J. F. Yang, L. N. LeMar, G. Zhang, A. Pervan, T. D. Murphey, M. S. Strano, *Faraday Discuss.* **2021**, *227*, 213.

[84] X. D. Zhuang, Y. Chen, G. Liu, B. Zhang, K. G. Neoh, E. T. Kang, C. X. Zhu, Y. X. Li, L. J. Niu, *Adv. Funct. Mater.* **2010**, *20*, 2916.

[85] A. H. Edwards, H. J. Barnaby, K. A. Campbell, M. N. Kozicki, W. Liu, M. J. Marinella, *Proc. IEEE* **2015**, *103*, 1004.

[86] Y. Chen, G. Liu, C. Wang, W. Zhang, R. W. Li, L. Wang, *Mater. Horizons* **2014**, *1*, 489.

[87] T. Fu, X. Liu, H. Gao, J. E. Ward, X. Liu, B. Yin, Z. Wang, Y. Zhuo, D. J. F. Walker, J. Joshua Yang, J. Chen, D. R. Lovley, J. Yao, *Nat. Commun.* **2020**, *11*, 1.

[88] T. McFarlane, Y. Bandera, B. Grant, B. Zdyrko, S. H. Foulger, J. Vilčáková, P. Sáha, J. Pfleger, *Adv. Electron. Mater.* **2020**, *6*, 2000042.

[89] W. Qian, X. Cheng, J. Zhou, J. He, H. Li, Q. Xu, N. Li, D. Chen, Z. Yao, J. Lu, *InfoMat* **2020**, *2*, 743.

[90] M. Qi, S. Cao, L. Yang, Q. You, L. Shi, Z. Wu, *Appl. Phys. Lett.* **2020**, *116*, DOI 10.1063/5.0003696.

[91] X. Feng, Y. Li, L. Wang, S. Chen, Z. G. Yu, W. C. Tan, N. Macadam, G. Hu, L. Huang, L. Chen, X. Gong, D. Chi, T. Hasan, A. V. Thean, Y. Zhang, K. Ang, *Adv. Electron. Mater.* **2019**, *5*, 1900740.

[92] M. Hempel, V. Schröder, C. Park, M. Xue, J. Park, T. Swager, J. Kong, T. Palacios, *SynCells - Electronic Microparticles for Sensing Applications*, Cambridge, MA, **2019**.

[93] C. W. Lee, J. M. Suh, H. W. Jang, *Front. Chem.* **2019**, *7*, 1.

[94] S. Ammu, V. Dua, S. R. Agnihotra, S. P. Surwade, A. Phulgirkar, S. Patel, S. K. Manohar, *J. Am. Chem. Soc.* **2012**, *134*, 4553.

[95] N. Yamazoe, G. Sakai, K. Shimanoe, *Catal. Surv. from Asia* **2003**, *7*, 63.

[96] V. S. Turkani, D. Maddipatla, B. B. Narakathu, B. J. Bazuin, M. Z. Atashbar, *Sensors Actuators A Phys.* **2018**, *279*, 1.

[97] X. Cao, X. Wei, G. Li, C. Hu, K. Dai, J. Guo, G. Zheng, C. Liu, C. Shen, Z. Guo, *Polymer (Guildf).* **2017**, *112*, 1.

[98] R. Nishikubo, A. Saeki, *J. Phys. Chem. Lett.* **2018**, *9*, 5392.

[99] N. Ghods, M. Krstic, *J. Dyn. Syst. Meas. Control* **2011**, *133*, DOI 10.1115/1.4003639.

[100] B. W. Bequette, *Process Dynamics: Modeling, Analysis, and Simulation*, Prentice Hall PTR, Upper Saddle River, NJ, **1998**.

[101] The MathWorks Inc., "Non-adiabatic continuous stirred tank reactor: MATLAB file modeling with simulations in Simulink®," can be found under https://www.mathworks.com/help/ident/ug/non-adiabatic-continuous-stirred-tank-reactor-matlab-file-modeling-with-simulations-in-simulink.html#d122e43522, **n.d.**

[102] Q. Jin, Y. Yang, J. A. Jackson, C. Yoon, D. H. Gracias, *Nano Lett.* **2020**, *20*, 5383.

[103] N. Kamaly, B. Yameen, J. Wu, O. C. Farokhzad, *Chem. Rev.* **2016**, *116*, 2602.

[104] V. P. Torchilin, *Nat. Rev. Drug Discov.* **2014**, *13*, 813.

[105] O. Veiseh, B. C. Tang, K. A. Whitehead, D. G. Anderson, R. Langer, *Nat. Rev. Drug Discov.* **2014**, *14*, 45.

[106] T. Hoeg-Jensen, *Mol. Metab.* **2020**, 101107.

[107] M. J. Webber, D. G. Anderson, *J. Drug Target.* **2015**, *23*, 651.

[108] J. T. Santini, M. J. Cima, R. Langer, *Nature* **1999**, *397*, 335.

[109] L. A. Villarruel Mendoza, N. A. Scilletta, M. G. Bellino, M. F. Desimone, P. N. Catalano, *Front. Bioeng. Biotechnol.* **2020**, *8*, 1.

[110] K. B. Sutradhar, C. D. Sumi, *Drug Deliv.* **2016**, *23*, 1.

[111] R. Farra, N. F. Sheppard, L. McCabe, R. M. Neer, J. M. Anderson, J. T. Santini, M. J. Cima, R. Langer, *Sci. Transl. Med.* **2012**, *4*, DOI 10.1126/scitranslmed.3003276.

[112] B. Zinger, L. L. Miller, *J. Am. Chem. Soc.* **1984**, *106*, 6861.

[113] J. M. Maloney, S. A. Uhland, B. F. Polito, N. F. Sheppard, C. M. Pelta, J. T. Santini, *J. Control. Release* **2005**, *109*, 244.

[114] Y. Li, H. L. H. Duc, B. Tyler, T. Williams, M. Tupper, R. Langer, H. Brem, M. J. Cima, *J. Control. Release* **2005**, *106*, 138.

[115] V. Pillay, T. S. Tsai, Y. E. Choonara, L. C. Du Toit, P. Kumar, G. Modi, D. Naidoo, L. K. Tomar, C. Tyagi, V. M. K. Ndesendo, *J. Biomed. Mater. Res. - Part A* **2014**, *102*, 2039.

[116] J. F. Yang, X. Gong, N. A. Bakh, K. Carr, N. F. B. Phillips, F. Ismail-Beigi, M. A. Weiss, M. S. Strano, *Diabetes* **2020**, *69*, 1815.

[117] M. Maheandiran, S. Mylvaganam, C. Wu, Y. El-Hayek, S. Sugumar, L. Hazrati, M. del Campo, A. Giacca, L. Zhang, P. L. Carlen, *PLoS One* **2013**, *8*, DOI 10.1371/journal.pone.0083168.

[118] N. A. Bakh, G. Bisker, M. A. Lee, X. Gong, M. S. Strano, *Adv. Healthc. Mater.* **2017**, *6*, 1.

[119] P. E. Cryer, S. N. Davis, H. Shamoon, *Diabetes Care* **2003**, *26*, 1902.

[120] A. GhavamiNejad, J. Li, B. Lu, L. Zhou, L. Lam, A. Giacca, X. Y. Wu, *Adv. Mater.* **2019**, *31*, 1901051.

[121] M. H. Smolensky, N. A. Peppas, *Adv. Drug Deliv. Rev.* **2007**, *59*, 828.

[122] M. D. Ruben, D. F. Smith, G. A. Fitzgerald, J. B. Hogenesch, *Science* **2019**, *365*, 547.

[123] Z. Wang, H. Wu, G. W. Burr, C. S. Hwang, K. L. Wang, Q. Xia, J. J. Yang, *Nat. Rev. Mater.* **2020**, *5*, 173.

[124] F. Barahona, M. Grötschel, M. Jünger, G. Reinelt, *Oper. Res.* **1988**, *36*, 493.

[125] G. G. E. Gielen, H. C. C. Walscharts, W. M. C. Sansen, *IEEE J. Solid-State Circuits* **1990**, *25*, 707.

[126] A. Pervan, T. D. Murphey, in *Proc. 13th Work. Algorithmic Found. Robot.*, **2018**.

[127] A. Censi, **2015**.

[128] A. Mirhoseini, A. Goldie, M. Yazgan, J. W. Jiang, E. Songhori, S. Wang, Y. J. Lee, E. Johnson, O. Pathak, A. Nazi, J. Pak, A. Tong, K. Srinivasa, W. Hang, E. Tuncer, Q. V. Le, J. Laudon, R. Ho, R. Carpenter, J. Dean, *Nature* **2021**, *594*, 207.

[129] S. Choi, S. H. Tan, Z. Li, Y. Kim, C. Choi, P.-Y. Chen, H. Yeon, S. Yu, J. Kim, *Nat. Mater.* **2018**, DOI 10.1038/s41563-017-0001-5.

[130] S. Goswami, S. P. Rath, D. Thompson, S. Hedström, M. Annamalai, R. Pramanick, B. R. Ilic, S. Sarkar, S. Hooda, C. A. Nijhuis, J. Martin, R. S. Williams, S. Goswami, T. Venkatesan, *Nat. Nanotechnol.* **2020**, *15*, 380.

[131] S. Goswami, D. Deb, A. Tempez, M. Chaigneau, S. P. Rath, M. Lal, Ariando, R. S. Williams, S. Goswami, T. Venkatesan, *Adv. Mater.* **2020**, *32*, 1.

[132] A. A. Bessonov, M. N. Kirikova, D. I. Petukhov, M. Allen, T. Ryhänen, M. J. A. Bailey, *Nat. Mater.* **2015**, *14*, 199.

[133] S. Y. Cho, X. Gong, V. B. Koman, M. Kuehne, S. J. Moon, M. Son, T. T. S. Lew, P. Gordiichuk, X. Jin, H.

D. Sikes, M. S. Strano, *Nat. Commun.* **2021**, *12*, 1.

[134] F. Fan, B. Zhang, Y. Cao, X. Yang, J. Gu, Y. Chen, *Nanoscale* **2017**, *9*, 10610.

[135] S. Brivio, G. Tallarida, D. Perego, S. Franz, D. Deleruyelle, C. Muller, S. Spiga, *Appl. Phys. Lett.* **2012**, *101*, 223510.

[136] F. Hui, M. Lanza, *Nat. Electron.* **2019**, *2*, 221.

[137] Y. Zuo, H. Lin, J. Guo, Y. Yuan, H. He, Y. Li, Y. Xiao, X. Li, K. Zhu, T. Wang, X. Jing, C. Wen, M. Lanza, *Adv. Electron. Mater.* **2020**, *6*, 1.

[138] F. N. Najm, *Circuit Simulation*, John Wiley & Sons, Inc., Hoboken, NJ, USA, **2010**.

[139] M. Sitti, *Mobile Microrobotics*, MIT Press, Cambridge, MA, **2017**.

Memristor circuits for colloidal robotics: Temporal access to memory, sensing, and actuation

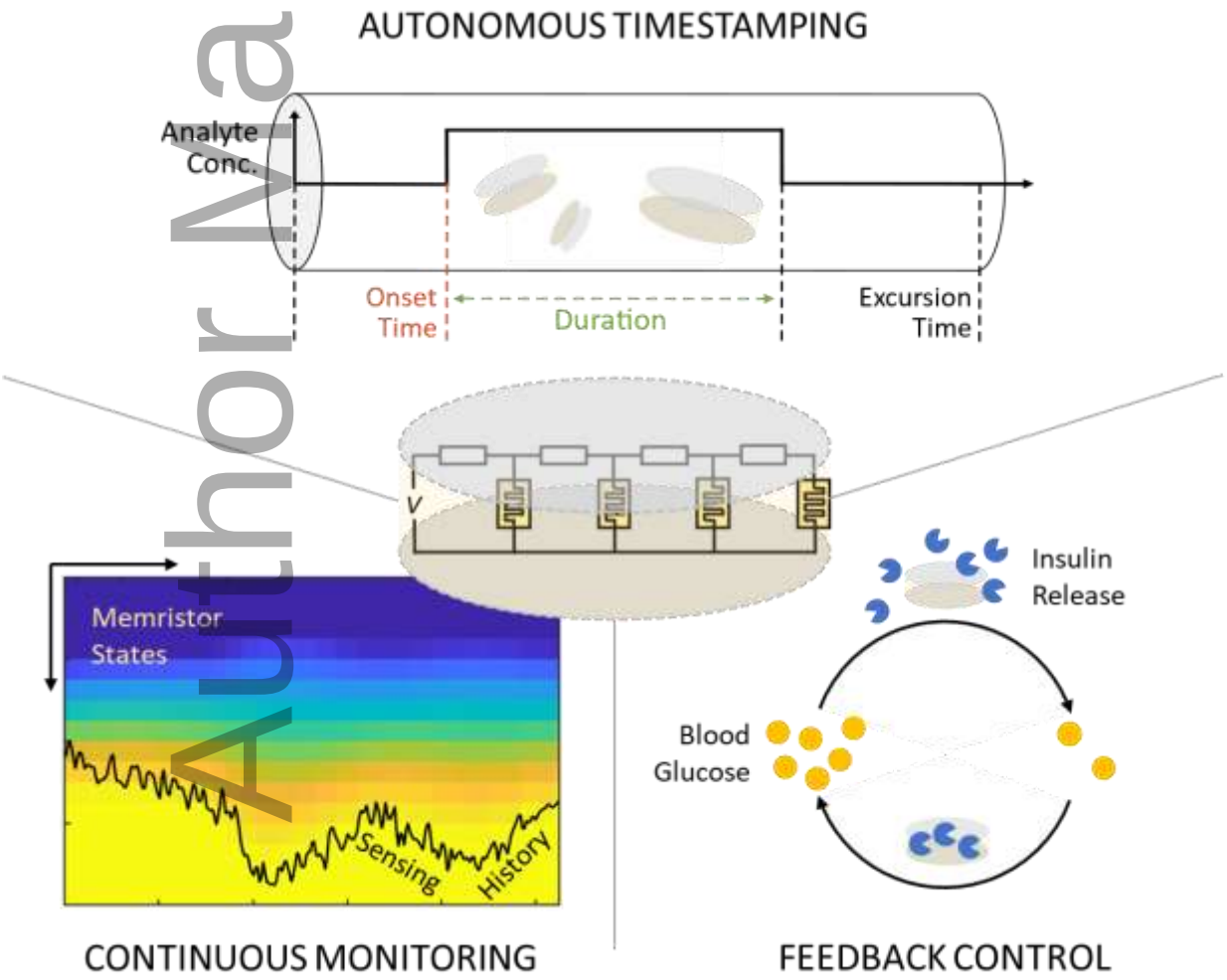

A memristor-based microrobotic circuit is introduced, which enables autonomous real-time use of on-board memory, sensing, and actuation. The robust design is validated against representative tasks requiring autonomy: tracking time, timestamping a rare event, cataloguing time-indexed data, and accessing the collected information for feedback-controlled response. Our computational work enables self-assembled and printed memristor arrays to perform tasks usually requiring complex circuits.